Check for updates

Hybrid nanocomposites of nanostructured Co_3O_4 interfaced with reduced/nitrogen-doped graphene oxides for selective improvements in electrocatalytic and/or supercapacitive properties†

Sheng Hu,‡[bcd] Erick L. Ribeiro,‡[bcd] Seyyed Ali Davari,[ac] Mengkun Tian,[b] Dibyendu Mukherjee [ID] *[abcd] and Bamin Khomami*[abd]

Performance enhancements in next-generation electrochemical energy storage/conversion devices require the design of new classes of nanomaterials that exhibit unique electrocatalytic and supercapacitive properties. To this end, we report the use of laser ablation synthesis in solution (LASiS) operated with cobalt as the target in graphene oxide (GO) solution in tandem with two different post-treatments to manufacture three kinds of hybrid nanocomposites (HNCs) namely, (1) Co_3O_4 nanoparticle (NP)/reduced graphene oxide (rGO), (2) Co_3O_4 nanorod (NR)/rGO, and (3) Co_3O_4 NP/nitrogen-doped graphene oxide (NGO). FTIR and Raman spectroscopic studies indicate that both chemical and charge-driven interactions are partially responsible for embedding the Co_3O_4 NPs/NRs into the various GO films. We tune the selective functionalities of the as-synthesized HNCs as oxygen reduction reaction (ORR) catalysts and/or supercapacitors by tailoring their structure–property relationships. Specifically, the nitrogen doping in the NP/NGO HNC samples promotes higher electron conductivity while hindering aggregation between 0D CoO NPs that are partially reshaped into Co_3O_4 nanocubes due to induced surface strain energies. Our results indicate that such interfacial energetics and arrangements lead to superior ORR electrocatalytic activities. On the other hand, the interconnecting 1D nanostructures in the NR/rGO HNCs benefit charge transport and electrolyte diffusion at the electrode–electrolyte interfaces, thereby promoting their supercapacitive properties. The NP/rGO HNCs exhibit intermediate functionalities towards both ORR catalysis and supercapacitance.

Introduction

The increasing global demand for clean and sustainable energy sources has triggered significant impetus towards the research and development of electrochemical energy storage/conversion systems such as proton/anion exchange membrane fuel cells (PEMFCs/AEMFCs) and supercapacitors.[1–5] Fuel cell devices typically require highly active and cost-effective catalysts to accelerate the rate-determining and sluggish oxygen reduction

a Department of Mechanical, Aerospace, & Biomedical Engineering, University of Tennessee, Knoxville, Tennessee, 37996, USA. E-mail: dmukherj@utk.edu; bkhomami@utk.edu; Tel: +1 86 5974 5309; +1 86 5974 2035

b Department of Chemical & Biomolecular Engineering, University of Tennessee, Knoxville, Tennessee, 37996, USA

c Nano-BioMaterials Laboratory for Energy, Energetics & Environment (nbmL-E3), University of Tennessee, Knoxville, Tennessee, 37996, USA

d Sustainable Energy Education & Research Center (SEERC), University of Tennessee, Knoxville, Tennessee, 37996, USA

† Electronic supplementary information (ESI) available. See DOI: 10.1039/c7ra05494g

‡ Erick L. Ribeiro and Sheng Hu contributed equally to this paper.

reactions (ORR) at the cathode.[6–8] To this end, efforts have been recently devoted to the synthesis of non-platinum group metal (non-PGM) electrocatalysts to replace the traditionally expensive Pt-based catalysts that are prone to extensive aggregation and loss of surface area during operation, especially under the prevalent alkaline/acidic operating conditions of PEMFCs/AEMFCs.[9,10] On the other hand, supercapacitors, including electrochemical double-layer capacitors (EDLC) and pseudo-capacitors, have concurrently gained prominence due to their superior power densities and longer life cycles comparing with typical batteries and fuel cells, and higher energy densities when compared to conventional dielectric capacitors.[4,11–14] Specifically, the EDLCs are driven by the electrostatic energy storage achieved via nanoscopic charge separation in a Helmholtz double layer at the matter–electrolyte interface. In comparison, pseudo-capacitors typically store electrical energy faradaically based upon the electron charge transfer between electrodes and electrolytes, where non-PGM electrocatalysts can also play critical roles in facilitating the charge transfer processes.

Graphene and reduced graphene oxide (rGO) have been well-characterized as the classical two-dimensional (2D) materials with unique honey-comb lattice structures that exhibit unique physicochemical properties along with high electrochemistry surface area and conductivity.[1,15–20] Additionally, efforts have been directed towards chemically reacting GO with nitrogen-containing species to synthesize nitrogen-doped GO (NGO) that are known to exhibit higher electron mobility and chemical compatibilities as compared to other metal/metal oxides dopants.[7,9,10,21–27] In turn, both rGO and NGO have been widely explored and reported as potentially excellent supporting materials for various catalytic systems as well as EDLC materials.[5,28–32]

A highly promising earth-abundant transition metal oxide, cobalt oxide (Co_3O_4)-based nanomaterials have gained prominence in recent years due to their relatively good ORR activities in alkaline conditions (specifically, for AEMFCs) along with outstanding pseudo-capacitance capabilities.[6,17,18,25,33,34] To this end, much recent research has been devoted to assembly of Co_3O_4 nanoparticles (NPs), nanorods (NRs), and nanosheets into rGO/NGO to form hybrid nanocomposites (HNCs).[7,25,26,35] The inherent strong coupling and consequent synergistic effects between the metal oxide nanostructures and rGO/NGO result in larger effective electrochemical surface areas and higher electron conductivity for the faradaic reactions to take place.[1,18,36–42] This, in turn, promotes a higher and more stable ORR catalytic activity as well as an enhanced capacitive capability that facilitates their behaviors as both EDLC and pseudocapacitors.[7,25,43–46] However, simple physical mixing of metal oxides and rGO/NGO would inevitably impede the charge transfer processes across the composite material for both ORR and capacitive performances due to the high electron resistivity at the interface.[17,47,48]

To address the abovementioned issue, researchers have typically resorted to chemical synthesis routes to assemble various heteronanostructures chemisorbed and/or embedded into 2D matrices such as graphene, GO, MoS_2, etc.[1,40,49] While such routes have been successfully used in the past to synthesize HNCs, they almost always involve complex multiple steps[50,51] and sometimes unwanted/harsh chemical and surfactants[52] that can be left behind as residues, thereby degrading the active interfacial areas for catalytic and charge transport pathways. To this end, we have recently reported the use of LASiS as well as LASiS in tandem with galvanic replacement reaction (GRR) as a facile and environmentally-clean route to manufacture diverse classes of heteronanostructures including Co_3O_4 NPs/NRs, single crystal β-Co(OH)$_2$ NPs, and Pt-based binary/ternary nanoalloys and nanocomposites.[53–56] The merit of LASiS stems from the extreme temperature and pressure inside the laser-induced plasma plume that facilitates the nucleation of seeding NPs from within a cavitation bubble and subsequent ultrafast reactions with the surrounding solution-phase species.[57–66] Furthermore, the charge screening effects arising from the high-density laser-induced plasma prevent the NP aggregations to a large extent without the use of any external surfactants/ligands. It is also noted that the kinetics of such reactions are driven by out-of-equilibrium thermodynamic conditions that promote the formation of nanomaterials in metastable phases.[53,61,67–70] Consequently, it becomes possible to further modify the structure/composition of various metastable products by tuning the appropriate experimental protocols.

Herein, we report the use of LASiS in conjunction with two different post-treatments to incorporate three types of cobalt oxide nanostructures into rGO/NGO sheets for synthesizing tailored HNCs. Our aim is to investigate the selective tuning of the ORR catalytic and/or supercapacitive properties of the HNCs *via* systematic synthesis–structure–property characterizations.

Experimental details

Synthesis of hybrid nanocomposites (HNCs)

LASiS procedure. All chemicals were purchased from Sigma-Aldrich. GO suspension was prepared by following the commonly practiced improved hummers method.[71] Co pellets were bought from Kurt J. Lesker (99.95% purity, 1/4″ diameter × 1/4″ height). LASiS experiments were carried out in an in-house built laser ablation cell equipped with facilities for simultaneous injection of solution-phase chemicals, temperature control as well as ultrasonication (details depicted in our earlier work[53,54]). Specifically, the freshly prepared GO solution with the concentration of 20 mg L^{-1} was bath-sonicated for 30 min before transferring into the LASiS cell through the injection unit. The target metal, while being rotated by a stepper motor at a uniform speed of 0.3 rpm, was ablated using an unfocused 1064 nm pulsed Nd-YAG laser (330 mJ per pulse, 10 Hz) for 3 min. The products were collected by centrifuging at 4700 rpm for 5 min. For LASiS in alkaline conditions, KOH (99.5%) was used to tune the solution pH to the desired alkaline condition (pH13).

Post-treatments. For the synthesis of all Co_3O_4/rGO HNCs, the products from centrifugation (precipitates) were heated at 250 °C under vacuum for 3 hours. For the production of all Co_3O_4/NGO HNCs, the precipitates were resuspended in 25 mL of deionized (DI) water, urea was then added at the ratio 100 : 1 (urea : GO). The mixture was sealed in a 50 mL Teflon-lined autoclave and held at 180 °C for 3 hours. The products were filtered and washed several times with DI-water. Finally, the dark powder obtained from the filtration was dried at 80 °C for 3 hours.

Characterizations

A Zeiss Libra 200MC monochromated transmission electron microscope (TEM) was used with an accelerating voltage of 200 kV for regular TEM characterizations along with selected area electron diffraction (SAED) and energy dispersive X-ray spectroscopy (EDX). The scanning electron microscopy (SEM) images were acquired using a Philips XL-30ESEM equipped with an energy dispersive X-ray spectroscopy. A Zetasizer (Make: Malvern; Model: nano ZS) was used for measuring zeta potentials of the colloidal solutions. The Co concentrations in the composites under study were measured *via* inductively coupled plasma optical emission spectroscopy (ICP-OES) (Make: Perkin

Elmer; Model: Optima 4300 DV) and our in-house developed quantitative laser-induced breakdown spectroscopy (Q-LIBS) as described elsewhere.[72-75] X-ray diffraction (XRD) was carried out on a Phillips X'Pert-Pro diffractometer equipped with a Cu Ka source at 45 kV and 40 mA. The Fourier transformed infrared (FTIR) spectrum was obtained using a Nicolet 6700 FT-IR Spectrometer at the wavenumber range of 400 to 3000 cm^{-1}. Raman spectra were acquired using an NT-MDT NTEGRA spectra with a 532 nm laser beam. Thermogravimetric analysis (TGA) were carried out under an air atmosphere using a Perkin Elmer Thermal Analyzer at a heating rate of 5 °C min^{-1}. AFM images were collected in the tapping mode on a Dimension ICON instrument from Veeco. X-ray photoelectron spectroscopy (XPS) data was collected using a SPECS Phoibos 150 analyzer with the Al K-alpha fluorescence line providing photon energy of 1486.7 eV. The overall energy resolution of the experiment was set to about 0.7 eV.

Electrochemical tests

The rotating disk electrode (RDE) setup was bought from Pine instrument company, LLC. A conventional, three-compartment electrochemical cell comprising a saturated double junction Ag/AgCl electrode as the reference electrode, and a platinum coil as the counter electrode were used for all the EC tests. All potentials in this work are reported in reference to the standard hydrogen electrode (SHE).

Oxygen reduction reaction (ORR) tests. A glassy carbon RDE with a diameter of 5 mm was used as the working electrode, 0.1 M KOH solution was used as the electrolyte. 20% Pt/C from BASF was used as the standard catalyst for all comparisons. For preparing the working electrode, 2 mg of the synthesized hybrid nanocomposites (HNCs) after the above-mentioned post-treatments were suspended in 0.5 mL ethanol and 25 μL of 5 wt% Nafion solution (Sigma-Aldrich, density 0.874 g mL^{-1}) via 30 min of ultrasonication. Thereafter, 25 μL of the prepared catalyst ink was coated on the RDE where the catalyst loading density was calculated to be ~500 μg cm^{-2}. For all ORR experiments, stable voltammogram curves were recorded after scanning for 15 cycles in the corresponding potential regions. The dynamics of the electron transfer process in ORR were analyzed through the rotating disk voltammetry (RDV) at different speeds based on the Koutecky–Levich (KL) equation:

$$\frac{1}{J} = \frac{1}{J_K} + \frac{1}{J_L} = \frac{1}{J_K} + \frac{1}{B\omega^{1/2}}$$

$$J_K = nFkC_0; \ B = 0.62nFC_0D_0^{2/3}\nu^{-1/6}$$

where J, J_K, and J_L are the measured, kinetic and diffusion limiting current densities respectively, n is the electron transfer number, F is the Faraday constant, C_0 and D_0 are the dissolved O_2 concentration the O_2 diffusion coefficient in the electrolyte respectively, ν is the electrode rotation rate in rpm. All Tafel plots were generated using the kinetic current J_K as determined from:

$$J_K = \frac{J \times J_L}{J_L - J}$$

Electrochemical supercapacitance measurements. The working electrode was prepared from the desired mixture of the Co_3O_4/rGO and/or Co_3O_4/NGO HNC samples (after post-treatments), acetylene black (Cabot), and polyvinylidene difluoride (PVDF, Aldrich) blend with a weight ratio of 8 : 1 : 1. The electrodes were fabricated by loading the blend onto the surface of nickel foam sheets, drying at 80 °C for 8 h, and pressing under 10 MPa for 5 s. The typical mass loading of the electrode active material was about ~3–5 mg. 6 M KOH solution was used as the electrolyte. Cyclic voltammetry (CV) measurements were conducted in a potential window of −0.15 to 0.35 V at the scanning rate of 20 mV s^{-1}. The charge–discharge tests were carried out at different current densities over a potential range of −0.1 to 0.35 V. Electrochemical impedance spectroscopy (EIS) was carried out on the same electrochemistry workstation in the frequency range from 0.05 Hz to 100 kHz for an open-circuit potential with 5 mV as the amplitude potential. The specific capacitance was calculated from the following equation:

$$C = \frac{I \times \Delta t}{\Delta V \times m} \left(\text{F } g^{-1}\right)$$

where C is the specific capacitance, I am the current density during discharging, m is the weight loading of the electroactive material.

Results and discussion

Structural characterizations

The GO flakes synthesized via the improved Hummer's method indicate lateral dimensions of ~1 μm, as shown in both AFM and SEM images in Fig. 1a–c respectively. The height profile in Fig. 1b for the corresponding cross-section (marked as the red line in Fig. 1a) indicates the average flake thickness to be ~1 nm that corresponds to 2–3 GO layers. Fig. 1d reveals a uniform dispersion for the as-synthesized GO flakes in the aqueous suspension, which aggregates instantly after the LASiS process (Fig. 1e) and in turn, easily precipitates upon centrifugation (Fig. 1f). Such aggregation arises largely due to the oppositely charged surfaces for the Co/CoO$_x$ NPs and GO flakes, as seen from the zeta potential measurements shown in ESI (EIS, Fig. S1†). Specifically, the Co/CoO$_x$ NPs from LASiS carry net effective positive charges in the Stern layer (a positive zeta potential of ~+32 mV), while the GO flakes carry net effective negative Stern layer charges (a negative zeta potential of ~−55 mV). Hence, the two species quickly attract each other during the LASiS step to neutralize the interfacial charges and in turn, form fluffy aggregates due to lack of charge stabilization. It needs to be borne in mind that the zeta potentials for both pure GO flakes and CoO$_x$ NPs being >+30 mV and <−30 mV respectively allow for the electrostatic stabilization of their respective aqueous suspensions.
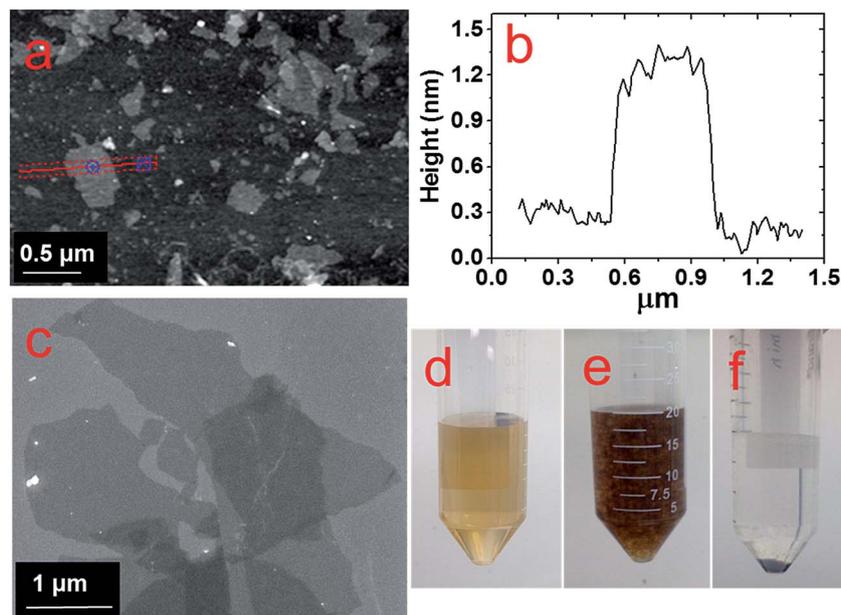
Fig. 1 AFM (a) and SEM (c) images of GO flakes prepared by improved hummer's method. (b) Height profile of one flake across the red line marked in (a); pictures of (d) pure GO suspension, (e) NP/rGO suspension right after LASiS, and (f) sample (e) after centrifugation.

In order to make better electrochemical supporting materials, the conductivity of the GO sheets in the as-synthesised CoO_x/GO nanocomposites are improved *via* two different reduction processes namely, (1) direct heating at 250 °C, and (2) nitrogen-doping (N-doping) to generate rGO and NGO respectively as the supporting matrices for the various Co_3O_4 nanostructures (as described in detail in the Experimental part). It needs to be mentioned here that the initial products from LASiS on Co are the metastable CoO and/or $Co(OH)_2$ crystals, both of which transform into Co_3O_4 NPs as the final product upon aging or heating, as also noted in our earlier work.[53] The SEM and TEM images in Fig. 2a–e indicate the various morphologies for the Co_3O_4/rGO HNCs made from the direct heating routes. For the pH7 case, Fig. 2a and b indicates the formation of uniformly distributed NPs in GO sheets. Here, the crystalline structures from electron diffraction pattern (inset in Fig. 1b) and lattice fringes from high-resolution TEM (HRTEM) images (Fig. 1c) confirm the NPs to be Co_3O_4 (enlarged image along with detailed crystalline structure identification can be found in Fig. S2 and Table S1 in ESI†). In contrast, for the pH13 case, Fig. 2d–f indicate the formation of a mixture of Co_3O_4 NPs and nanorods (NRs) uniformly distributed on rGO matrices (also indicated by the inset in Fig. 2e and demonstrated in Fig. S2 and Table S1 in ESI†). Such formation of Co_3O_4 NRs is attributed to the breakdown of $Co(OH)_2$ hexagonal single crystals, as discussed in detail in our previous work.[53] Besides, the EDX mappings in Fig. 2g–j for the Co_3O_4 NP/rGO HNC samples further confirm the even distribution of each element/species in the HNCs. In our second reduction route, the N-doping procedure (as detailed in Experimental section) on the CoO_x/GO samples made from LASiS at pH7 conditions generates NH_3 molecules that quickly react with surface functional groups on

the GO and consequently induce the formation of Co_3O_4/NGO HNCs. Specifically, in this case, it is clearly observed from Fig. 3a–c that during the N-doping process, some of the spherical CoO_x NPs get structurally re-arranged into Co_3O_4 nanocubes indicating relatively less agglomeration. We attribute this to the possible spatial confinement of the NPs within ∼5–6 layers of the NGO, as seen from HRTEM images in Fig. 3b and c, that re-distributes the surface energy during the crystalline growth of the Co_3O_4 NPs. Such spatial confinements from few layers of graphitic shells have also been reported in previous literature.[76] Meanwhile, it should also be pointed out that in this case, the NPs show a relatively poorer coverage on NGO (Fig. 3a) as compared to the surface coverage for the Co_3O_4/rGO HNCs. For ease of understanding, from here onwards, we refer to the aforementioned three products as NP/rGO (pH7), NR/rGO (pH13) and NP/NGO (pH7, N-doping) respectively. The weight ratios of Co_3O_4 : C were estimated from Q-LIBS measurements and confirmed by ICP-OES to be 3 : 1 for both NP/rGO and NP/NGO, and 3 : 2 for NR/rGO as reported in EIS (Fig. S6 and S7†). The XRD patterns for the various HNC products under study are shown in Fig. 4. The pure GO exhibits a distinct peak at ∼12°, which corresponds to GO (002) and implies an interlayer spacing of about 0.76 nm, while the two small peaks at ∼34° and 45° are due to trace amounts of impurities. The absence of the GO (002) peak after the incorporation of Co_3O_4 nanostructures (NPs/NRs) suggest a disruption of the GO lattice stacking as well as partial reduction during the reaction with seeding Co NPs. After the N-doping process, a broad peak located at ∼25° is exhibited for the NP/NGO sample, suggesting a successful reduction of GO. The NP/rGO samples before heating (NP/rGO-RT) indicate very weak peaks for $Co(OH)_2$ (001) at ∼19°, which quickly disappears after calcination at 250 °C
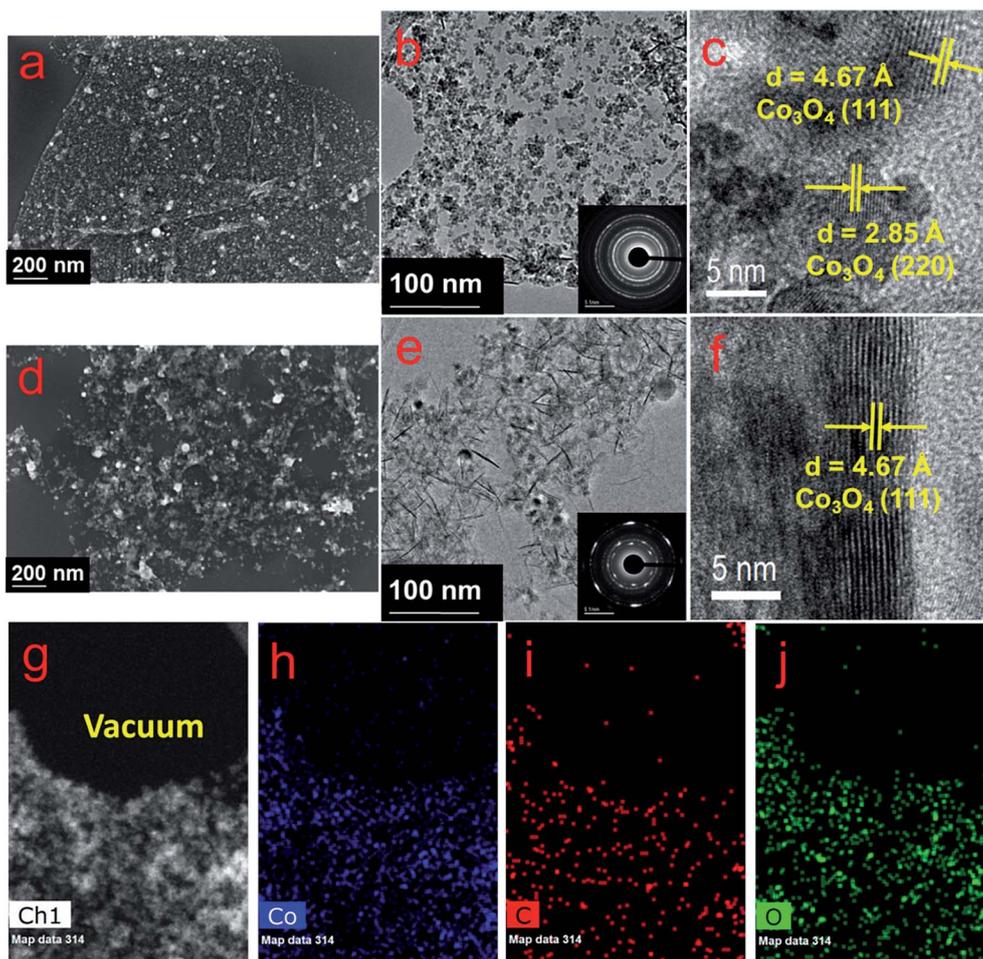
Fig. 2   SEM (a and d) and TEM/HRTEM (b, c, e and f) images for the Co$_3$O$_4$ NP/rGO HNCs prepared at pH7 (a–c) and Co$_3$O$_4$ NR/rGO HNCs prepared at pH13 (b, e and f) conditions. The insets in (b and e) reveal the corresponding SAED patterns. (g–j) STEM image of the Co$_3$O$_4$ NP/rGO sample prepared at pH7 (g) and the corresponding EDX mappings for Co (h), C (i) and O (j) elements.

(NP/rGO-250) due to the relative instability of Co(OH)$_2$ at high temperatures. A similar phenomenon is also observed for the NR/rGO samples, except that a huge Co(OH)$_2$ (001) peak appears before the heating (NR/rGO-RT). This is clearly attributed to the reaction between the seeding Co NPs from LASiS and the concentrated solution phase OH$^-$ from the alkaline conditions (pH13). The transformation of these metastable Co(OH)$_2$

nanocrystals into Co$_3$O$_4$ under alkaline conditions lead to their selective crystalline growth as nanorods. In consequence, the emergence of a Co$_3$O$_4$ (311) peak is seen after heating the samples to 250 °C (NR/rGO-250). These observations have also been reported and explained in details in our earlier work.[53] Finally, we would like to mention that neither NP/rGO nor NP/NGO samples show any Co$_3$O$_4$ peaks in the XRD pattern due to
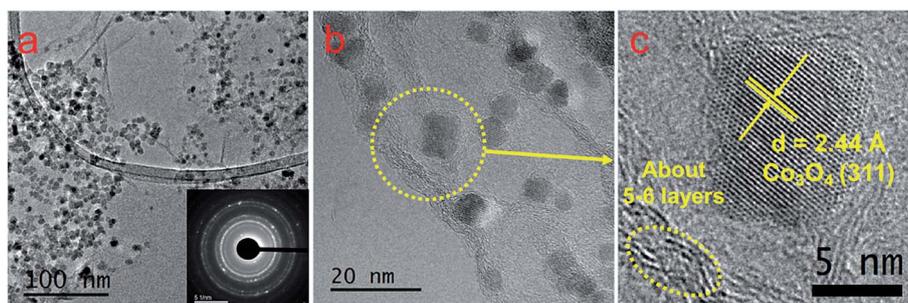

Fig. 3   TEM (a) and HRTEM (b and c) images of the Co$_3$O$_4$ NP/NGO HNCs. The inset in (a) reveals the corresponding SAED patterns.
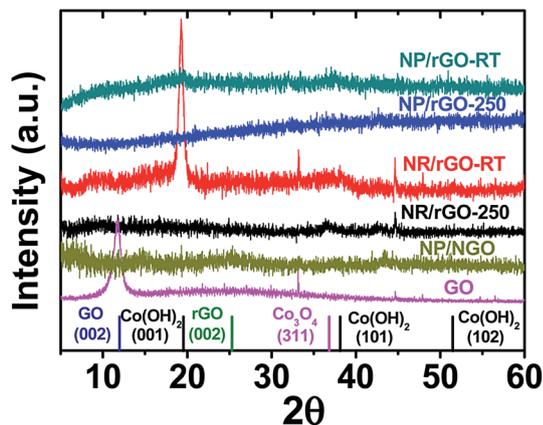
Fig. 4 Comparison of XRD patterns for various HNC samples under study. The standard peak position for each species is shown by the vertical lines at the bottom.

the relatively small NP sizes as well as the weak crystallization processes, which is as a result of the non-equilibrium ultrafast quenching of the laser-induced plasma plume in water where the NPs are generated.

Interfacial characterizations

In this section, the formations of rGO/NGO and Co_3O_4 in the aforementioned HNC samples along with their interfaces are further investigated by FTIR, Raman spectroscopy and XPS. The FTIR spectra of NP/rGO and NR/rGO at different heating temperatures are recorded in Fig. 5a and b respectively. Both as-synthesized samples (RT case) exhibit a broad peak at ~3400

cm^{-1} that correspond to the O–H stretching vibration, along with several sharp peaks located at 1650 cm^{-1}, 1391 cm^{-1} 1250 cm^{-1}, 1060 cm^{-1} representing C=C, COOH, C–O–C and C–O bonding respectively.[36,50,77] The last two peaks located at lower wavenumbers, i.e., 665 and 570 cm^{-1} are assigned to the stretching vibration of Co^{3+}–O and Co^{2+}–O bonds.[36,50,77] Upon heating (150 °C and 250 °C cases), the O–H, COOH and C–O peaks disappear, while the C=C peak is found to shift to a lower wavenumber of ~1610 cm^{-1}, and a small C–O–C peak starts to emerge at 1060 cm^{-1}. Such observations indicate and confirm the thermal reduction of GO. The Co–O peaks, however, indicate a successive reduction of the 665 and 570 cm^{-1} stretching peaks along with the formation of a tail at ~500 cm^{-1} after the heating, which is possibly due to the solid phase reaction between Co/CoO and GO that forms a more complex structure. For the sake of comparison, another set of HNC sample was prepared by carrying out LASiS on Co in water first, followed by heating the solution overnight until CoO_x gets fully oxidized into Co_3O_4, and then physically mixing it with GO at the same Co_3O_4 : GO weight ratio as the NP/rGO sample (3 : 1). With this technique, no chemical reaction occurs between Co_3O_4 and GO. The FTIR result for this sample is shown in Fig. 5c. Clearly, much stronger peaks for the Co–O bonding is seen with no tail after heating, suggesting that the Co_3O_4 NPs are only physically absorbed onto GO. This confirms our earlier hypothesis regarding the possible reactions between Co/CoO and GO during both the LASiS step and the subsequent vacuum heating that result in the formation of more complex Co–rGO structures exhibiting lower intensities for the Co–O stretching. The Raman spectra in Fig. 5d for all the Co_3O_4-containing HNC samples detect the four distinct peaks at 677, 517, 470 and 193 cm^{-1} that
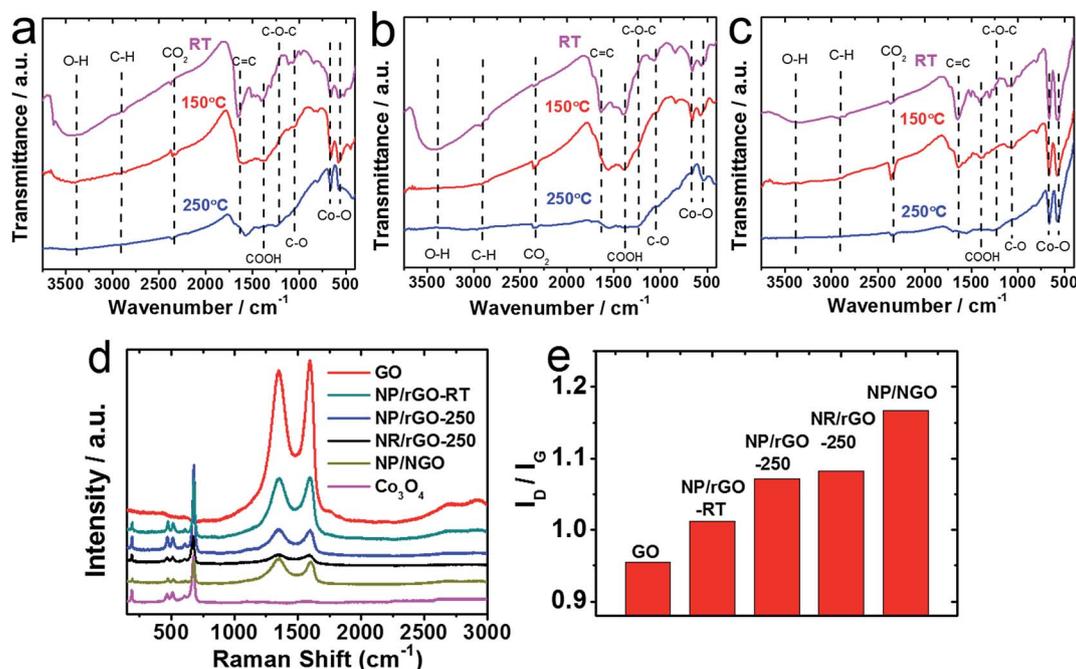

Fig. 5 (a–c) FTIR results for (a) NP/rGO, (b) NR/rGO, and (c) physically mixed HNCs heated to different temperatures; (d) Raman spectra of the as-synthesized products; (e) the fitting results for the intensity ratios of D-band (~1350 cm^{-1}) to G-band (~1650 cm^{-1}) from (d).

correspond to the A_{1g} and F_{2g} modes of Co_3O_4.[39,78,79] Alternately, all the GO-containing HNC samples exhibit two broad peaks at 1351 and 1604 cm^{-1} that are assigned to the carbon D band and G band vibrations for GO. Specifically, the D peak is related to the mode of the k-point phonons of A_{1g} symmetry while the G peak corresponds to the E_{2g} phonon of C_{sp^2} atoms.[36,38,50] The D/G intensity ratios (I_D/I_G) for all the HNC samples were calculated and summarized in Fig. 5e, where a high value indicates better exfoliation,[39] more disorder/defects,[80] and reduced oxygenated functional groups.[50] It is clearly seen that both thermal reduction and N-doping effectively increases the I_D/I_G, with the NP/NGO sample showing the highest value of 1.16. The reduction of GO is further characterized by the XPS results shown in Fig. 6b, e and h, where the C–O characteristic peak obtained from C 1s fitting is found to significantly decrease after N-doping/heating. Meanwhile, the survey spectrum for NP/NGO (Fig. 6d) reveals a distinctive N 1s peak at 400 eV in comparison to NP/GO (Fig. 6a), confirming the effective N doping for this sample. The doped N atoms are further found to mostly exist in pyrrolic or pyridinic forms,[81] as shown in Fig. 6g. Finally, the Co 2p peaks (Fig. 6c, f and i) indicate the coexistence of Co^{2+}

and Co^{3+} oxidation state, confirming the formation of Co_3O_4 for all the NP samples, with NP/rGO showing a relatively higher Co_3O_4 ratio which can be attributed to the high temperature heating process.

Functional characterizations

Two types of electrochemical properties, namely, ORR electro-catalytic activity and supercapacitive property are evaluated and compared for the as-synthesized HNCs. The ORR polarization curves in Fig. 7a indicates that the NP/NGO HNC exhibits the best ORR activity among all the samples in terms of the onset potential and diffusion-limited current, followed by the NP/rGO, Co_3O_4/C, and NR/rGO samples. Specifically, the onset potential and diffusion-limited current for NP/NGO HNCs (-0.15 V $vs.$ SHE, and -5 mA cm^{-2} respectively) are very close to the corresponding values for commercial Pt/C ORR catalysts (-0.08 V $vs.$ SHE, and -5.6 mA cm^{-2}). Furthermore, the Tafel plots in Fig. 7b for the kinetic-diffusion region of the ORR polarization curves indicate the Tafel slope for NP/NGO samples ($\sim$45 mV dec^{-1}) to be even lower than that for Pt/C (48 mV dec^{-1}) samples. This suggests a faster charge transfer rate for
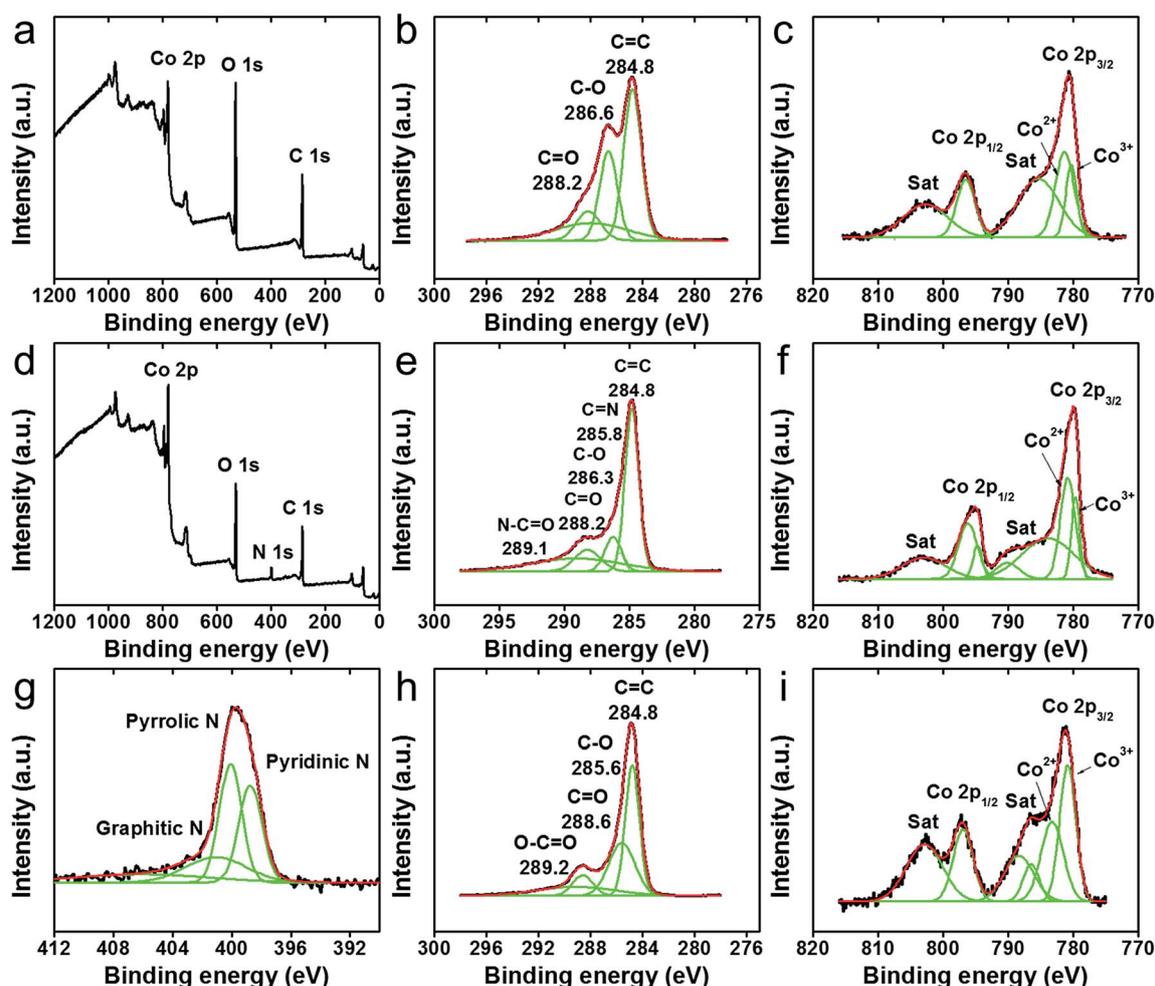

Fig. 6   XPS results indicating the survey spectra (a and d), C 1s (b, e and h), Co 2p (c, f and i) and N 1s (g) for: NP/GO (a–c), NP/NGO (d–g) and NP/rGO (h and i).
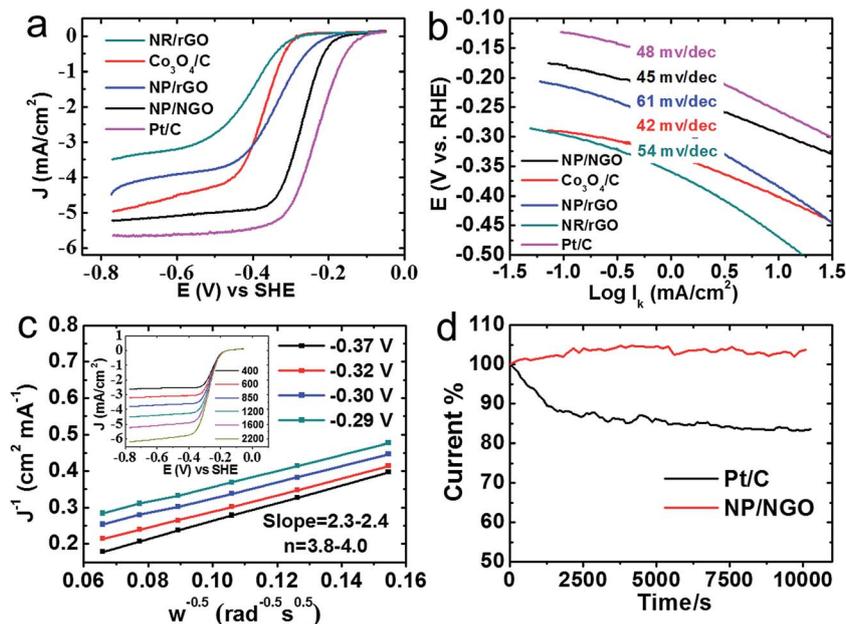
Fig. 7 Electrochemistry data for the as-synthesized HNCs compared to standard Pt/C for ORR electrocatalytic activities using: (a) ORR polarization curves in 0.1 M KOH electrolyte saturated with dissolved O_2 at 1600 rpm and scan rate of 10 mV s^{-1}; (b) Tafel plots from (a); (c) Koutecky–Levich plots from RDV data (inset) for the NP/NGO HNC at different potentials (0.29–0.37 V) indicate four electron transport process; (d) stability comparison for NP/NGO HNC and standard Pt/C via CA tests.

the ORR kinetics of the NP/NGO HNC samples. Typical Koutecky–Levich plots extracted from rotating disk voltammogram at different rotation speeds, as shown in Fig. 7c and the inset enable quantification of electron transfer numbers for the ORR catalysis by the NP/NGO HNCs. The results clearly indicate a near four electron transport process in the mixed kinetic-diffusion region with the potential ranging from −0.29 V to −0.37 V. Finally, the NP/NGO HNC electrocatalyst is also found to be more stable than the Pt/C. As shown in Fig. 7d, the chronoamperometry test run for 10 000 s at −0.25 V indicates negligible changes in the current density for the NP/NGO samples, whereas the standard Pt/C samples see a dramatic decline by ∼16% from the starting point value. The superior ORR activity for NP/NGO can be attributed to the N-doping process that endows NGO with ultrahigh electron mobility along with less agglomerated Co_3O_4 NPs that are devoid of any interfacial contaminants from surfactants/ligand, thereby providing a larger electroactive surface area.

The supercapacitor performance for the synthesized HNCs is shown in Fig. 8. The two redox peaks located at the midpoint potentials of ∼0.15 and ∼0.28 V on the CV curves (Fig. 8a) correspond to the following two faradaic reactions for Co_3O_4:

$$Co_3O_4 + H_2O + OH^- \Leftrightarrow 3CoOOH + e^-$$

$$CoOOH + OH^- \Leftrightarrow CoO_2 + H_2O + e^-$$

Fig. 8b reveals the discharge curves at 1 A g^{-1} from −0.1 to 0.35 V for various samples under study. All HNCs exhibit longer discharge time, i.e., better capacitive performance than both pure Co_3O_4 (159 F g^{-1}) and rGO (68.4 F g^{-1}), with NR/rGO showing the largest capacitance of 269 F g^{-1} that is

comparable with values reported in other literatures for similar NP/rGO systems,[18,40,82,83] followed by NP/NGO (213 F g^{-1}) and NP/rGO (196 F g^{-1}). Fig. 8c illustrates the complete charge–discharge curves for NR/rGO at different scan rates. The curves are found to be symmetrical which exhibit the typical characteristics for an ideal supercapacitor. Finally, the electrode–electrolyte interface properties were characterized via EIS measurements (see Experimental section) with the resultant Nyquist plots shown in Fig. 8d and the corresponding equivalent circuit illustrated in Fig. S9 in ESI.† At the high-frequency region, the intercept at real part (Z') denotes the intrinsic resistance of the electrode, electrolyte as well as their contact resistance (R_e).[38,40] Pure Co_3O_4 is found to exhibit the largest R_e among all the samples, thereby impairing its specific capacitance. R_{ct} stands for charge-transfer resistance, which is affected by the aforementioned faradaic reactions. NR/rGO exhibits the lowest R_{ct} of 0.37 Ω, followed by Co_3O_4 (0.52 Ω), NP/rGO (0.87 Ω), NP/NGO (1.43 Ω), and rGO (4.31 Ω). The linear part of the low-frequency region of the Nyquist plot corresponds to the Warburg impedance, which represents the diffusion of electrolyte to the electrode materials. NR/rGO exhibits the most vertical slope, indicating the best electrolyte diffusion efficiency.[38,40] Thus, the better supercapacitive properties for NR/rGO, when compared to the other samples studied here, can be possibly ascribed to its interconnecting nanostructures comprising both NRs and NPs that lower the charge-transfer resistance and meanwhile promote the electrolyte diffusion rate at the interface. Qualitatively, it can be deduced from Fig. 8d that although NP/NGO shows the smallest R_e among all HNCs that promotes the charge transfer for ORR catalysis, the larger R_{ct} hinders their capacitive capabilities. This is probably due to the relatively poorer coverage of Co_3O_4 NPs on NGO,
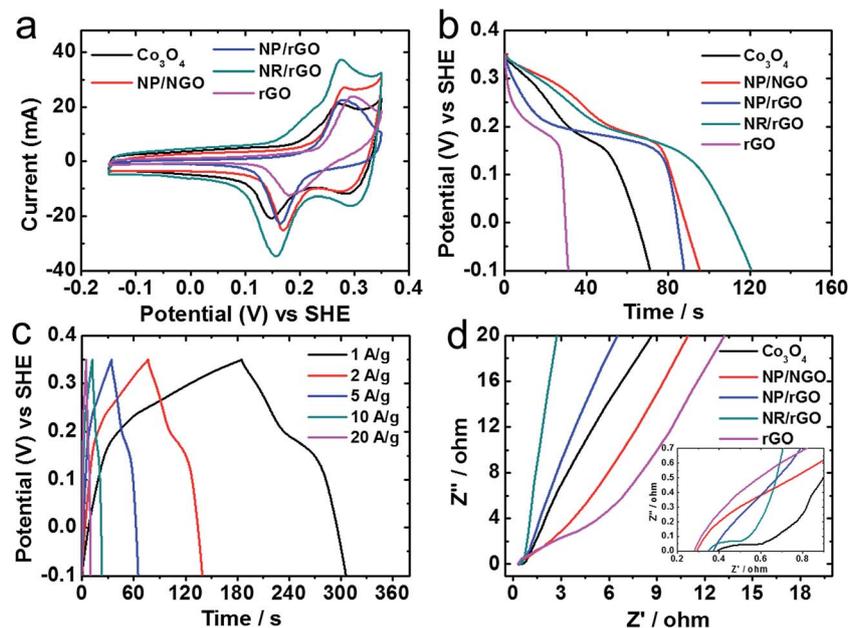
Fig. 8 Electrochemistry data showing capacitive properties for the as-synthesized products. (a) CV scans at 20 mV s^{-1}; (b) comparison of discharge curves at the scan rate of 1 A g^{-1}; (c) charge–discharge curves for NR/rGO at various rates (A g^{-1}); (d) Nyquist plots from EIS measurements. The inset shows an enlarged image at the high frequency region.

resulting in more NGO exposing to the surface, as demonstrated earlier in the TEM images in Fig. 3. In comparison, NP/rGO shows the expected intermediate activities for both ORR and supercapacitance.

Synthesis–structure relations: a discussion

Finally, we summarize the formation mechanism for the three types of HNCs under different LASiS conditions as depicted in Fig. 9. In general, laser ablation on the CO target induces the formation of a plasma containing Co species which nucleates within the propagating cavitation bubble. Once the bubble collapses, the seeding Co NPs go through ultrasonic quenching

at the liquid–bubble interface and meanwhile react with both water and GO flakes. This results in the formation of cobalt oxides embedded in rGO due to the primary reduction reactions at the bubble–liquid interface. The embedding process could be both chemically and charge driven, as demonstrated earlier in the FTIR and Raman results. The initial metal oxide products from LASiS in the alkaline condition (pH13) involve a mixture of CoO NPs, Co_3O_4 NRs and $Co(OH)_2$ hexagonal NPs, which further transform into interconnecting nanostructures comprising Co_3O_4 NPs and NRs upon thermal heating, and are responsible for the enhanced supercapacitive properties. On the contrary, at pH7 conditions, only CoO NPs are initially formed
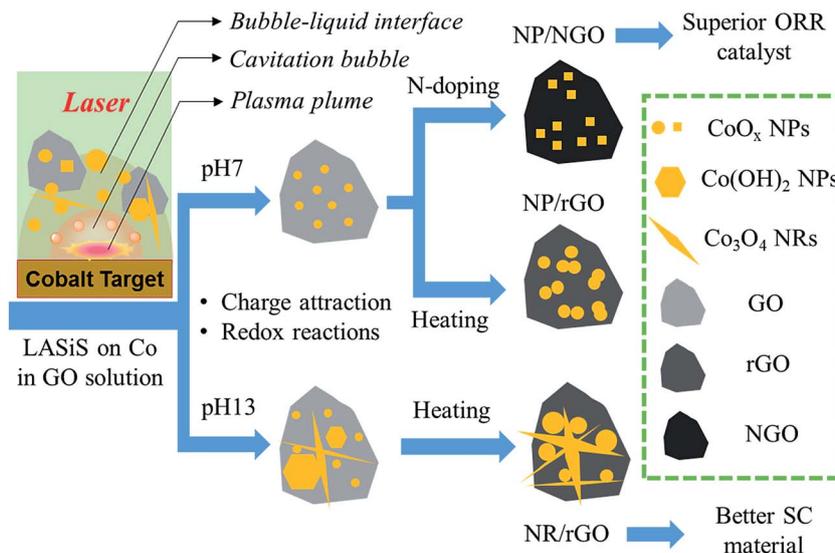

Fig. 9 Schematic diagram summarizing the formation of the three types of Co–GO HNCs under different synthesis conditions.

that are found to transfer into Co_3O_4 NPs upon heating. These Co_3O_4 NPs exhibit more uniform distribution on rGO than when formed *via* N-doping, albeit with a higher degree of agglomeration. The N-doping process endows the NGO with a higher conductivity, while partially reshaping the metastable CoO NPs into Co_3O_4 nanocubes with less agglomeration that is believed to eventually benefit their ORR catalytic activities.

Conclusions

In summary, three types of 0D-2D interfaced HNCs, namely, NP/rGO, NR/rGO and NP/NGO were manufactured *via* laser ablation synthesis in solution (LASiS) in tandem with two different post-treatments. The synthesized HNC samples were systematically characterized for their selective applications as ORR catalysts and/or supercapacitive materials. Detailed structural and interfacial characterizations reveal the embedment of the nanomaterials into GO to be both chemically and charge driven. Functional characterizations indicate that the NP/NGO HNC samples exhibit the best ORR activity that is comparable to the commercial Pt/C. This is ascribed to the higher electron mobility and conductivity arising from the N-doped GO (NGO) matrix along with the dispersion of isolated Co_3O_4 NPs devoid of any interfacial surfactants/ligands that provide enhanced electroactive surface areas. On the other hand, the NR/rGO samples indicate the highest supercapacitive activities resulting from interpenetrating nanostructures in the rGO matrix that benefit both charge transfer and electrolyte diffusion at the electrode interface. Finally, as expected from the aforementioned observations, the NP/rGO samples display mediocre bifunctional activities for both the applications. The ability to tune selective bi-functionalities in such tailored HNCs provide future pathways for the rational design of efficient fuel cell and/or battery electrodes from 0D–2D interfaced nanomaterials.

Acknowledgements

References

1 Q. Y. Liao, N. Li, S. X. Jin, G. W. Yang and C. X. Wang, *ACS Nano*, 2015, **9**, 5310–5317.

2 S. Hu, O. Dyck, H. Chen, Y.-c. Hsiao, B. Hu, G. Duscher, M. Dadmun and B. Khomami, *RSC Adv.*, 2014, **4**, 27931–27938.

3 M. Zhi, C. Xiang, J. Li, M. Li and N. Wu, *Nanoscale*, 2013, **5**, 72–88.

4 H. Yan, J. Bai, J. Wang, X. Zhang, B. Wang, Q. Liu and L. Liu, *CrystEngComm*, 2013, **15**, 10007–10015.

5 S. P. Wu, R. Xu, M. J. Lu, R. Y. Ge, J. Iocozzia, C. P. Han, B. B. Jiang and Z. Q. Lin, *Adv. Energy Mater.*, 2015, **5**, 1500400.

6 T. Odedairo, X. C. Yan, J. Ma, Y. L. Jiao, X. D. Yao, A. J. Du and Z. H. Zhu, *ACS Appl. Mater. Interfaces*, 2015, **7**, 21373–21380.

7 Z. J. Jiang and Z. Jiang, *Sci. Rep.*, 2016, **6**, 27081.

8 H. Tao, C. Yan, A. W. Robertson, Y. Gao, J. Ding, Y. Zhang, T. Ma and Z. Sun, *Chem. Commun.*, 2017, **53**, 873–876.

9 A. Pendashteh, J. Palma, M. Anderson and R. Marcilla, *Appl. Catal., B*, 2017, **201**, 241–252.

10 Y. Hou, Z. H. Wen, S. M. Cui, S. Q. Ci, S. Mao and J. H. Chen, *Adv. Funct. Mater.*, 2015, **25**, 872–882.

11 X. Zhou, X. Shen, Z. Xia, Z. Zhang, J. Li, Y. Ma and Y. Qu, *ACS Appl. Mater. Interfaces*, 2015, **7**, 20322–20331.

12 H. Ma, J. He, D. B. Xiong, J. Wu, Q. Li, V. Dravid and Y. Zhao, *ACS Appl. Mater. Interfaces*, 2016, **8**, 1992–2000.

13 X. Feng, J. Zhou, L. Wang, Y. Li, Z. Huang, S. Chen, Y. Ma, L. Wang and X. Yan, *New J. Chem.*, 2015, **39**, 4026–4034.

14 J. Zhou, J. Song, H. Li, X. Feng, Z. Huang, S. Chen, Y. Ma, L. Wang and X. Yan, *New J. Chem.*, 2015, **39**, 8780–8786.

15 Q. X. Feng, X. G. Li, J. Wang and A. M. Gaskov, *Sens. Actuators, B*, 2016, **222**, 864–870.

16 Y. L. Zheng, P. Li, H. B. Li and S. H. Chen, *Int. J. Electrochem. Sci.*, 2014, **9**, 7369–7381.

17 Y. G. Liu, Z. Y. Cheng, H. Y. Sun, H. Arandiyan, J. P. Li and M. Ahmad, *J. Power Sources*, 2015, **273**, 878–884.

18 L. Wang, D. L. Wang, J. S. Zhu and X. S. Liang, *Ionics*, 2013, **19**, 215–220.

19 X. Y. Zhou, J. J. Shi, Y. Liu, Q. M. Su, J. Zhang and G. H. Du, *Electrochim. Acta*, 2014, **143**, 175–179.

20 J. Zhang, Z. Dong, X. Wang, X. Zhao, J. Tu, Q. Su and G. Du, *J. Power Sources*, 2014, **270**, 1–8.

21 X. L. Li, H. L. Wang, J. T. Robinson, H. Sanchez, G. Diankov and H. J. Dai, *J. Am. Chem. Soc.*, 2009, **131**, 15939–15944.

22 X. J. Cui, Y. H. Li, S. Bachmann, M. Scalone, A. E. Surkus, K. Junge, C. Topf and M. Beller, *J. Am. Chem. Soc.*, 2015, **137**, 10652–10658.

23 K. Kumar, C. Canaff, J. Rousseau, S. Arrii-Clacens, T. W. Napporn, A. Habrioux and K. B. Kokoh, *J. Phys. Chem. C*, 2016, **120**, 7949–7958.

24 L. F. Lai, J. R. Potts, D. Zhan, L. Wang, C. K. Poh, C. H. Tang, H. Gong, Z. X. Shen, L. Y. Jianyi and R. S. Ruoff, *Energy Environ. Sci.*, 2012, **5**, 7936–7942.

25 T. Liu, Y. F. Guo, Y. M. Yan, F. Wang, C. Deng, D. Rooney and K. N. Sun, *Carbon*, 2016, **106**, 84–92.

26 T. T. Sun, L. B. Xu, S. Y. Li, W. X. Chai, Y. Huang, Y. S. Yan and J. F. Chen, *Appl. Catal., B*, 2016, **193**, 1–8.

27 S. Peng, H. Jiang, Y. Zhang, L. Yang, S. Wang, W. Deng and Y. Tan, *J. Mater. Chem. A*, 2016, **4**, 3678–3682.

28 Q. Li, N. Mahmood, J. H. Zhu, Y. L. Hou and S. H. Sun, *Nano Today*, 2014, **9**, 668–683.

29 H.-W. Wang, Z.-A. Hu, Y.-Q. Chang, Y.-L. Chen, Z.-Y. Zhang, Y.-Y. Yang and H.-Y. Wu, *Mater. Chem. Phys.*, 2011, **130**, 672–679.

30 J. M. Xu, J. S. Wu, L. L. Luo, X. Q. Chen, H. B. Qin, V. Dravid, S. B. Mi and C. L. Jia, *J. Power Sources*, 2015, **274**, 816–822.

31 Q. Ke, Y. Liao, S. Yao, L. Song and X. Xiong, *J. Mater. Sci.*, 2016, **51**, 2008–2016.

32 J. L. Yang, J. J. Wang, Y. J. Tang, D. N. Wang, X. F. Li, Y. H. Hu, R. Y. Li, G. X. Liang, T. K. Sham and X. L. Sun, *Energy Environ. Sci.*, 2013, **6**, 1521–1528.

33 V. H. Nguyen and J. J. Shim, *Mater. Lett.*, 2015, **139**, 377–381.

34 Q. Su, J. Zhang, Y. Wu and G. Du, *Nano Energy*, 2014, **9**, 264–272.

35 Y. Y. Liang, Y. G. Li, H. L. Wang, J. G. Zhou, J. Wang, T. Regier and H. J. Dai, *Nat. Mater.*, 2011, **10**, 780–786.

36 T. T. Nguyen, V. H. Nguyen, R. K. Deivasigamani, D. Kharismadewi, Y. Iwai and J. J. Shim, *Solid State Sci.*, 2016, **53**, 71–77.

37 G. Y. He, J. H. Li, H. Q. Chen, J. Shi, X. Q. Sun, S. Chen and X. Wang, *Mater. Lett.*, 2012, **82**, 61–63.

38 C. C. Xiang, M. Li, M. J. Zhi, A. Manivannan and N. Q. Wu, *J. Power Sources*, 2013, **226**, 65–70.

39 B. Wang, Y. Wang, J. Park, H. Ahn and G. X. Wang, *J. Alloys Compd.*, 2011, **509**, 7778–7783.

40 Y. Q. Zou, I. A. Kinloch and R. A. W. Dryfe, *ACS Appl. Mater. Interfaces*, 2015, **7**, 22831–22838.

41 V. H. Nguyen and J.-J. Shim, *J. Power Sources*, 2015, **273**, 110–117.

42 V. H. Nguyen, C. Lamiel and J.-J. Shim, *Electrochim. Acta*, 2015, **161**, 351–357.

43 F. Bonaccorso, L. Colombo, G. Yu, M. Stoller, V. Tozzini, A. C. Ferrari, R. S. Ruoff and V. Pellegrini, *Science*, 2015, **347**, 1246501.

44 J. Ji, L. L. Zhang, H. Ji, Y. Li, X. Zhao, X. Bai, X. Fan, F. Zhang and R. S. Ruoff, *ACS Nano*, 2013, **7**, 6237–6243.

45 G. He, L. Wang, H. Chen, X. Sun and X. Wang, *Mater. Lett.*, 2013, **98**, 164–167.

46 Q. Qiu, Y. Chen, J. Xue, J. Zhu, Y. Fu, G. He and H. Chen, *Ceram. Int.*, 2017, **43**, 2226–2232.

47 S. Faraji and F. N. Ani, *J. Power Sources*, 2014, **263**, 338–360.

48 H. Wang and H. Dai, *Chem. Soc. Rev.*, 2013, **42**, 3088–3113.

49 D. Liang, Z. Tian, J. Liu, Y. Ye, S. Wu, Y. Cai and C. Liang, *Electrochim. Acta*, 2015, **182**, 376–382.

50 S. K. Ujjain, G. Singh and R. K. Sharma, *Electrochim. Acta*, 2015, **169**, 276–282.

51 S. M. Choi, M. H. Seo, H. J. Kim and W. B. Kim, *Synth. Met.*, 2011, **161**, 2405–2411.

52 R. Pocklanova, A. K. Rathi, M. B. Gawande, K. K. R. Datta, V. Ranc, K. Cepe, M. Petr, R. S. Varma, L. Kvitek and R. Zboril, *J. Mol. Catal. A: Chem.*, 2016, **424**, 121–127.

53 S. Hu, C. Melton and D. Mukherjee, *Phys. Chem. Chem. Phys.*, 2014, **16**, 24034–24044.

54 S. Hu, M. Tian, E. L. Ribeiro, G. Duscher and D. Mukherjee, *J. Power Sources*, 2016, **306**, 413–423.

55 S. Hu, G. Goenaga, C. Melton, T. A. Zawodzinski and D. Mukherjee, *Appl. Catal., B*, 2016, **182**, 286–296.

56 S. Hu, K. Cheng, E. L. Ribeiro, K. Park, B. Khomami and D. Mukherjee, *Catal. Sci. Technol.*, 2017, **7**, 2074–2086.

57 R. Z. Li, R. Peng, K. D. Kihm, S. Bai, D. Bridges, U. Tumuluri, Z. Wu, T. Zhang, G. Compagnini, Z. Feng and A. Hu, *Energy Environ. Sci.*, 2016, **9**(4), 1458–1467.

58 J. Lam, J. Lombard, C. Dujardin, G. Ledoux, S. Merabia and D. Amans, *Appl. Phys. Lett.*, 2016, **108**, 074104.

59 A. Matsumoto, A. Tamura, T. Honda, T. Hirota, K. Kobayashi, S. Katakura, N. Nishi, K.-i. Amano, K. Fukami and T. Sakka, *J. Phys. Chem. C*, 2015, **119**, 26506–26511.

60 P. Liu, H. Cui, C. X. Wang and G. W. Yang, *Phys. Chem. Chem. Phys.*, 2010, **12**, 3942–3952.

61 H. B. Zeng, X. W. Du, S. C. Singh, S. A. Kulinich, S. K. Yang, J. P. He and W. P. Cai, *Adv. Funct. Mater.*, 2012, **22**, 1333–1353.

62 E. Jiménez, K. Abderrafi, R. Abargues, J. L. Valdés and J. P. Martínez-Pastor, *Langmuir*, 2010, **26**, 7458–7463.

63 S. Scaramuzza, M. Zerbetto and V. Amendola, *J. Phys. Chem. C*, 2016, **120**, 9453–9463.

64 D. Zhang, B. Gökce and S. Barcikowski, *Chem. Rev.*, 2017, **117**(5), 3990–4103.

65 A. Letzel, B. Gökce, P. Wagener, S. Ibrahimkutty, A. Menzel, A. Plech and S. Barcikowski, *J. Phys. Chem. C*, 2017, **121**(9), 5356–5365.

66 A. De Giacomo, M. Dell'Aglio, A. Santagata, R. Gaudiuso, O. De Pascale, P. Wagener, G. C. Messina, G. Compagnini and S. Barcikowski, *Phys. Chem. Chem. Phys.*, 2013, **15**, 3083–3092.

67 S. Scaramuzza, S. Agnoli and V. Amendola, *Phys. Chem. Chem. Phys.*, 2015, **17**(42), 28076–28087.

68 M. E. Povarnitsyn, T. E. Itina, P. R. Levashov and K. V. Khishchenko, *Phys. Chem. Chem. Phys.*, 2013, **15**, 3108.

69 V. Amendola and M. Meneghetti, *Phys. Chem. Chem. Phys.*, 2013, **15**, 3027–3046.

70 N. G. Semaltianos, S. Logothetidis, N. Frangis, I. Tsiaoussis, W. Perrie, G. Dearden and K. G. Watkins, *Chem. Phys. Lett.*, 2010, **496**, 113–116.

71 D. C. Marcano, D. V. Kosynkin, J. M. Berlin, A. Sinitskii, Z. Sun, A. Slesarev, L. B. Alemany, W. Lu and J. M. Tour, *ACS Nano*, 2010, **4**, 4806–4814.

72 S. A. Davari, S. Hu, E. L. Ribeiro and D. Mukherjee, *MRS Adv.*, 2017, 1–6, DOI: 10.1557/adv.2017.303.

73 S. A. Davari, S. Hu and D. Mukherjee, *Talanta*, 2017, **164**, 330–340.

74 S. A. Davari, S. Hu, R. Pamu and D. Mukherjee, *J. Anal. At. Spectrom.*, 2017, DOI: 10.1039/c7ja00083a.

75 S. A. Davari, S. Masjedi, Z. Ferdous and D. Mukherjee, *J. Biophotonics*, 2017, DOI: 10.1002/jbio.201600288.

76 S. Roy, R. Bajpai, N. Koratkar and D. S. Misra, *Carbon*, 2015, **85**, 406–413.

77 S. O. Huang, Y. H. Jin and M. Q. Jia, *Electrochim. Acta*, 2013, **95**, 139–145.

78 X. L. Sun, Z. Q. Jiang, C. X. Li, Y. Y. Jiang, X. Y. Sun, X. N. Tian, L. J. Luo, X. G. Hao and Z. J. Jiang, *J. Alloys Compd.*, 2016, **685**, 507–517.

79 H. Kim, D. H. Seo, S. W. Kim, J. Kim and K. Kang, *Carbon*, 2011, **49**, 326–332.

80 S. Saha, M. Jana, P. Samanta, N. C. Murmu, N. H. Kim, T. Kuila and J. H. Lee, *RSC Adv.*, 2014, **4**, 44777–44785.

81 L. Tang, R. Ji, X. Li, K. S. Teng and S. P. Lau, *J. Mater. Chem. C*, 2013, **1**, 4908.

82 S. Maiti, A. Pramanik and S. Mahanty, *CrystEngComm*, 2016, **18**, 450–461.

83 Y. Zhang, C. Sun, P. Lu, K. Li, S. Song and D. Xue, *CrystEngComm*, 2012, **14**, 5892–5897.